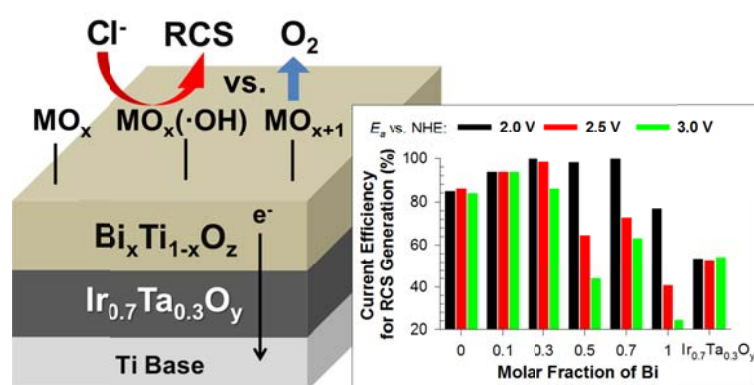


Chapter 5

BI_xTI_{1-x}O_z FUNCTIONALIZED HETERO-JUNCTION ANODE WITH AN ENHANCED REACTIVE CHLORINE GENERATION EFFICIENCY IN DILUTE AQUEOUS SOLUTIONS



ABSTRACT

New $\text{Ir}_{0.7}\text{Ta}_{0.3}\text{O}_y/\text{Bi}_x\text{Ti}_{1-x}\text{O}_z$ hetero-junction anodes have been developed and characterized for reactive chlorine species (RCS) generation in dilute aqueous solution (50 mM NaCl). The primary objective was to control the electro-stationary speciation of hydrous metal oxides between hydroxyl radical ($>\text{MO}_x(\cdot\text{OH})$) and higher valence-state oxides ($>\text{MO}_{x+1}$). An underlying layer of the mixed-metal oxide, $\text{Ir}_{0.7}\text{Ti}_{0.3}\text{O}_y$, was synthesized to serve as a primary ohmic contact and electron shuttle. Binary thin films of $\text{Bi}_x\text{Ti}_{1-x}\text{O}_z$ were prepared from the thermal decomposition of an aqueous solution mixture of Ti/Bi complexes. With these core components, the measured current efficiency for RCS generation (η_{RCS}) was enhanced where the values observed for $x = 0.1$ or 0.3 were virtually twice of the η_{RCS} of the $\text{Ir}_{0.7}\text{Ti}_{0.3}\text{O}_y$ anode. At the same time, the rates of RCS generation were enhanced by a factor of 20 – 30%. Partial substitution of Ti with Bi results in a positive shift in surface charge allowing for stronger interaction with anions as confirmed by FTIR-ATR analysis. A kinetic model to describe the formate ion degradation showed that an increasing fraction of Bi in the composite promotes a redox transition of $>\text{MO}_x(\cdot\text{OH})$ to $>\text{MO}_{x+1}$. In accelerated life tests under conditions corresponding to a service life of 2 years under an operational current density of 300 A m^{-2} , dissociation of Ti component from $\text{Ir}_{0.7}\text{Ta}_{0.3}\text{O}_y/\text{TiO}_2$ was found to be minimal, while BiO_x in the surface layers undergoes oxidation and a subsequent dissolution.

5.1. INTRODUCTION

We developed new hetero-junction mixed-metal oxides anodes, which allow for enhanced reactive chlorine generation in dilute aqueous solution in terms of current (energy) efficiency. The outer surface of the hetero-junction anodes is functionalized with $\text{Bi}_x\text{Ti}_{1-x}\text{O}_z$ layers which provide elevated electro-stationary concentration of adsorbed hydroxyl radical, while the underlying $\text{Ir}_{0.7}\text{Ta}_{0.3}\text{O}_y$ layer serves both as ohmic contact and electron shuttle. This study demonstrates that the surficial binary metal oxides layers, prepared through traditional thermal decomposition of aqueous Ti and Bi complex solutions, not only shift the heterogeneous kinetics and selectivity but also reduce a loss of the precious element (*e.g.*, Iridium) under long-term operation.

Dimensionally stable anodes (DSAs) consisting of mixed-metal oxides containing either IrO_2 or RuO_2 as core components have been widely deployed for industrial chlorine production (chloro-alkali processes),¹ energy storage into molecular H_2 (polymer exchange membrane electrolysis),^{2,3} and high-salinity wastewater treatment processes,^{4,5} among many other uses. Drawbacks to long-term application include the high materials cost of Ir and Ru as well as their instability relative to conversion to IrO_4^{2-} and RuO_4 under operational anodic potential bias.⁶ In recent years, strategies to promote the mass normalized activities of IrO_2 or RuO_2 have relied on increasing electro-active surface area via either quantum sizing the crystalline structure^{3,7} or elevation in thin film porosity^{1,2} by modern material preparation techniques. The use of mixed-metal oxides anodes has been extended to composites containing Ta_2O_5 ,⁶ TiO_2 ,^{6,8-10} SnO_2 ,^{11,12} ZrO_2 ,⁶ CeO_2 ,^{8,9} and Sb_2O_5 ^{11,12} as a secondary or tertiary component, most often focusing on enhancement in

stability or conductivity. Nevertheless, for a couple of decades, IrO₂-Ta₂O₅ (Ir:Ta = 7:3) and RuO₂-TiO₂ (Ru:Ti = 3:7) combinations remain the best composition accepted for an industrial application with respect to oxygen evolution reaction (OER) and chlorine evolution reaction (CIER), respectively.^{1,2,6}

Another challenge to point out in this regard is that the Pt-group metal oxides with the lowest over-potential for OER also exhibit outstanding electro-catalytic activities for chlorine generation. The competition between OER and CIER is due to their competition for active surface sites (*e.g.*, surface coordinated reactive oxygen species).¹³ Upon an electrical potential gradient across the anode/electrolyte interface, hydrous metal oxides have been known to produce physi-sorbed hydroxyl radicals ($>MO_x(\cdot OH)$) and, by further oxidative transition, higher oxides ($>MO_{x+1}$).^{4,5,14} As a rule of thumb, the surface-bound $>MO_x(\cdot OH)$ is believed to prefer reactions with electron-donating substances adsorbed on the surface, whereas liberation of active oxygen chemi-sorbed to a higher-oxidation-state central metal into molecular O₂ would be favored for $>MO_{x+1}$.¹⁴ The quasi-stationary distribution between $>MO_x(\cdot OH)$ and $>MO_{x+1}$ is primarily determined by the enthalpy change in lower ($>MO_x$) to higher ($>MO_{x+1}$) oxides transition or the binding energy of active oxygen.^{13,15,16} In this context, volcano plots have been used to interpret the electrochemical activities of variable types of metal oxide.¹⁵ Recent density functional theory calculations suggested that the volcano type relations for OER and CIER overlap while the highest activity is seen with RuO₂ followed by IrO₂.^{13,16}

The additives are often used to control the electrolyte composition (*i.e.*, the activities of chloride ion, water, and proton) and to minimize various scavenging reactions.¹⁷ The

selectivity toward a desired product is also contingent upon the speciation of surficial reactive oxygen species which, in turn, is mostly determined by the specific composition of the anode.^{4,5} Relatively low metal-oxygen bond strengths for PbO_2 , SnO_2 , and TiO_2 are known to facilitate reactions between $>\text{MO}_x(\cdot\text{OH})$ and electron donating substrates (*e.g.*, organics and chloride ion). As a result, metal oxides located at the left-hand side of a typical volcano plot show considerably high current efficiencies (selectivities of electron transfer), in spite of a large kinetic barrier (and energy consumption) for initial activation of $>\text{MO}_x$. On the contrary, $>\text{MO}_x(\cdot\text{OH})$ sites are readily quenched by redox transition of metal ions in case of IrO_2 - or RuO_2 -based mixed metal oxides with relatively low OER over-potentials. Therefore, the degradation of organic waste products on metal oxides near the apex of the volcano plot is primarily due to homogeneous reactions with reactive chlorine species (RCS) that are generated from $>\text{MO}_{x+1}$. In this case, the current generation from OER is often comparable or dominating that from ClER in dilute aqueous solutions.

Among several beneficial aspects of hetero-junction fabrication of catalytic thin film, a shift in heterogeneous kinetics can be anticipated by surface modification¹⁸ to enhance the selectivity towards the reaction of interest. TiO_2 in water lead to the formation of surface-bound hydroxyl radical, $>\text{Ti}(\cdot\text{OH})$, by trapping photo-chemically generated electrons and holes under illumination or with an applied potential bias equal to or greater than the bandgap energy.¹⁹ TiO_2 provides active sites for hydroxyl radical formation with limited transition to $>\text{MO}_{x+1}$.²⁰ On the other hand, Bi_2O_3 is known to have excellent pseudo-capacitance capability in the water splitting potential region and dielectric permittivity for use in Faradaic supercapacitors.^{21,22} Extraordinary oxide ion conductivity

attributed to intrinsic disordered oxygen vacancies and high polarizability by the presence of a $6s^2$ lone pair in Bi(III) allows Bi_2O_3 to be used as a solid oxide fuel cell electrolyte.²³ The electrochemical nature of Bi_2O_3 appears to be suitable for $>\text{MO}_x$ formation and OER.²⁴

In this paper, we report on the electrochemical activity and stability of $\text{Ir}_{0.7}\text{Ti}_{0.3}\text{O}_y/\text{Bi}_x\text{Ti}_{1-x}\text{O}_z$ hetero-junction anodes and their potential applications for electrochemical water and wastewater treatment. A systematic parametric study was undertaken in order to determine the effects of nominal molar fraction of Bi in $\text{Bi}_x\text{Ti}_{1-x}\text{O}_z$ functionalities on RCS generation efficacies during the course of potentiostatic electrolysis of dilute aqueous solutions with circum-neutral pH.

5.2. EXPERIMENTAL SECTION

5.2.1. $\text{Ir}_{0.7}\text{Ti}_{0.3}\text{O}_y/\text{Bi}_x\text{Ti}_{1-x}\text{O}_z$ Hetero-junction Anode Preparation. The hetero-junction semiconductor anodes were prepared by sequential thermal decomposition methods. Ti metal sheets ($3 \times 2 \text{ cm}^2$, 0.5 mm thickness) were pretreated by sand-blast, 50 V/V% acetone degreasing, and etching in boiling 10 M/V% oxalic acid right before fabrication. $\text{Ir}_{0.7}\text{Ta}_{0.3}\text{O}_y$ layers were prepared by brushing precursor (70 mM H_2IrCl_6 + 30 mM TaCl_5 in 1:1 ethanol and isopropanol) on both sides of Ti base, drying at 80 °C (10 min) and annealing at 525 °C (10 min). The electrodes underwent five more repetitive sequences and further heat treatment at 525 °C for 1 h as a final annealing, ending up with catalysts loading of 0.64 mg cm^{-2} on average. Aqueous titanium-glycolate complex was prepared from hydroxo-peroxo method,²⁵⁻²⁷ with proper modifications. In a typical recipe, titanium butoxide (250 mM of final concentration) and glycolic acid (375 mM) were added into a

relevant amount of water. The resulting precipitates were re-dissolved with 30 W/W% H_2O_2 (ca. 40% of final precursor volume). Exothermic reactions with a presence of dark red color appeared with vigorous generations of CO_2 and O_2 bubbles. In order to adjust the pH to be circum-neutral, a small aliquot of concentrated NH_4OH (ca. 3.5% of final precursor volume) was added. The color quickly changed into yellow with the pH adjustment while mild bubble generations (including N_2) continued with a decay of residual H_2O_2 . Aqueous Bi solutions were prepared by dissolving 250 mM bismuth citrate in 750 mM NH_4OH solutions. The resulting precursors of Ti and Bi were mixed together for preparation of $\text{Bi}_x\text{Ti}_{1-x}\text{O}_z$ layers with variable nominal molar fraction of Bi ($x = 0, 0.1, 0.3, 0.5, 0.7, 1$). Analogous thermal decomposition procedures were carried out on top of the $\text{Ir}_{0.7}\text{Ta}_{0.3}\text{O}_y$ anode with annealing temperature at 425 °C. The mass loading of outer $\text{Bi}_x\text{Ti}_{1-x}\text{O}_z$ layer ranged from 0.51 to 1.4 mg cm^{-2} , depending on the precursor composition (x). The prepared electrodes were cleaned with dilute acetone and a large amount of deionized water before electro-analytical and physic-chemical characterization.

5.2.2. Electroanalysis. The electrochemical reactor employed throughout this study consisted of an anode under investigation, a stainless steel cathode in parallel ($3 \times 2 \text{ cm}^2$, 5 mm distance), and a Ag/AgCl/Sat. KCl reference electrode (Basi Inc.) in a one compartment cell (working volume of 60 mL). The Vycor® glass tip of the reference electrode was located 3 mm apart from the center of the anode. Applied anodic potential (E_a) from a potentiostat (SP-50, BioLogic) was converted to the normal hydrogen electrode (NHE) scale by $E_a(\text{NHE}) = E_a(\text{Ag/AgCl}) + 0.197 \text{ V}$. Cyclic voltammetry (CV) data in stirred 50 mM NaCl solutions (three consecutive cycles without open-circuit resting) were recorded in the range of E_a from 0.2 to 1.0 V at the scan rate of 20 mV sec^{-1} .

The quasi-stationary polarization data from 0.8 to 2.5 V were also collected with the scan rate of 5 mV sec⁻¹. Before each electrochemical experiment, open circuit potentials of anode and cathode were monitored for 30 min. The ohmic resistances were measured before and after each experiment by a current interruption method with current bias of 200 mA.

5.2.3. Potentiostatic RCS Generation and Formate Ion Degradation. The generation rate and current efficiency of RCS generation were estimated during potentiostatic electrolysis in 50 mM NaCl solutions under several different E_a (2.0, 2.5, and 3.0 V). The RCS concentration was measured by DPD (N,N-diethyl-p-phenylenediamine) reagent at a fixed time interval (2 min) three times with proper dilutions. The relatively low reaction time was intended to minimize an occurrence of chlorine species with higher oxidation states (ClO_3^- , ClO_4^-).²⁸ The current efficiency for the RCS generation was estimated by the following equation:

$$\eta_{\text{RCS}} = \frac{2VF d[\text{Cl}_{\text{DPD}}]}{I dt} \quad (5.1)$$

where, V is electrolyte volume (0.06 L), F is Faraday constant (96485.3 C mol⁻¹), $[\text{Cl}_{\text{DPD}}]$ is the concentration of RCS (M), I is current (A), and t is electrolysis time (sec). In order to assess the contribution of $>\text{MO}_x(\cdot\text{OH})$ on the RCS generation, formate ion was chosen as a probe compound for the surficial hydroxyl radical. Potentiostatic electrolysis experiments were performed in 50 mM NaCOOH solutions for 1 h. The $[\text{HCOO}^-]$ was measured for periodically collected samples using ion chromatography (Dionex, USA) with anion-exchange column (Ionpac AS 19).

5.2.4. Surface Characterization. After finishing the electrochemical experiments, anodes were cut into half pieces, each of which was subject to the physicochemical surface analysis and accelerated life test, respectively. The horizontal or cross-sectional morphology were observed by ZEISS 1550VP field emission scanning electron microscopy (SEM), while elemental compositions were analyzed by Oxford X-Max SDD X-ray energy dispersive spectrometer (EDS) system either in point-and-identification or mapping mode. X-ray diffraction (XRD) profiles were collected using an X'pert MD (Panalytical) diffractometer with Cu-K radiation. Thermo-Scientific Nicolet™ iS™50 Fourier transform infrared spectroscopy (FTIR) was used to characterize surface functionalities. Hetero-junction anodes were held on attenuated total reflectance (ATR) unit in contact either with deionized water or 1 M NaClO₄ solutions.

5.2.5. Accelerated Life Test. The stabilities of the Ir_{0.7}Ta_{0.3}O_y/Bi_xTi_{1-x}O_z hetero-junction anodes with variable molar fraction of Bi (x) were compared using accelerated life tests. Each hetero-junction anode sandwiched with a stainless steel cathode (0.5 × 2 cm², 3 mm distance) was immersed in 1 M NaClO₄ solution in a conical tube. Neware Battery Testing System powered the galvanostatic (current density= 1 A cm⁻²) electrolysis in each test cell. The electrolyte was replaced periodically (3 to 5 h interval), and dissociated amounts of Ti, Bi and Ir in the electrolyte were quantified by Agilent inductivity coupled plasma-mass spectrometry (ICP-MS).

5.3. RESULTS

5.3.1. Physico-chemical Properties. Figure 5.1 shows SEM images of the Ir_{0.7}Ta_{0.3}O_y/Bi_xTi_{1-x}O_z hetero-junction anodes with variable molar fraction of Bi (x) after

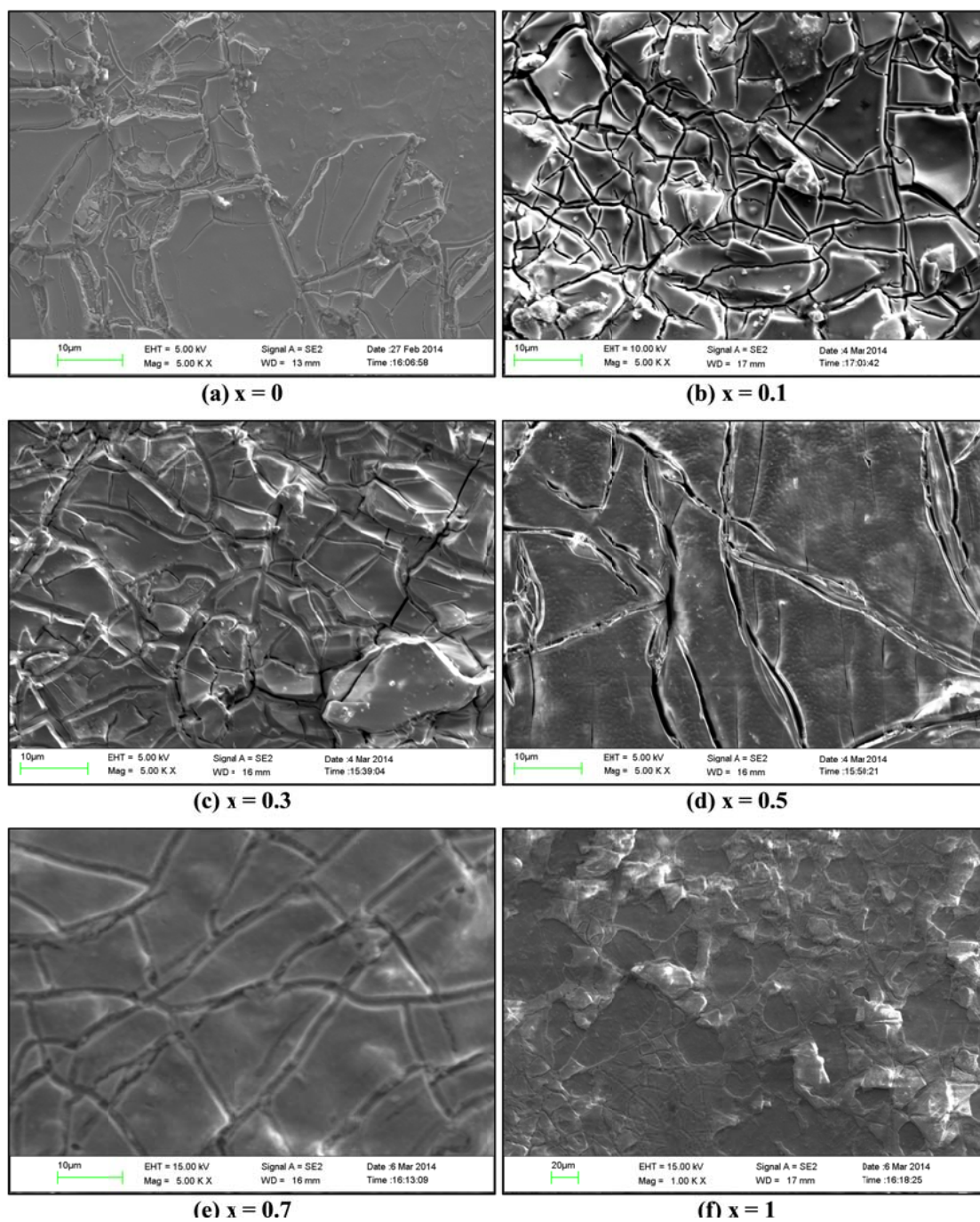


Figure 5.1. Scanning Electron Microscopy (SEM) images of horizontal view for $\text{Ir}_{0.7}\text{Ta}_{0.3}\text{O}_y/\text{Bi}_x\text{Ti}_{1-x}\text{O}_z$ hetero-junction anode with variable molar fraction of Bi with magnification of $\times 5000$ (a – e) or $\times 1000$ (f).

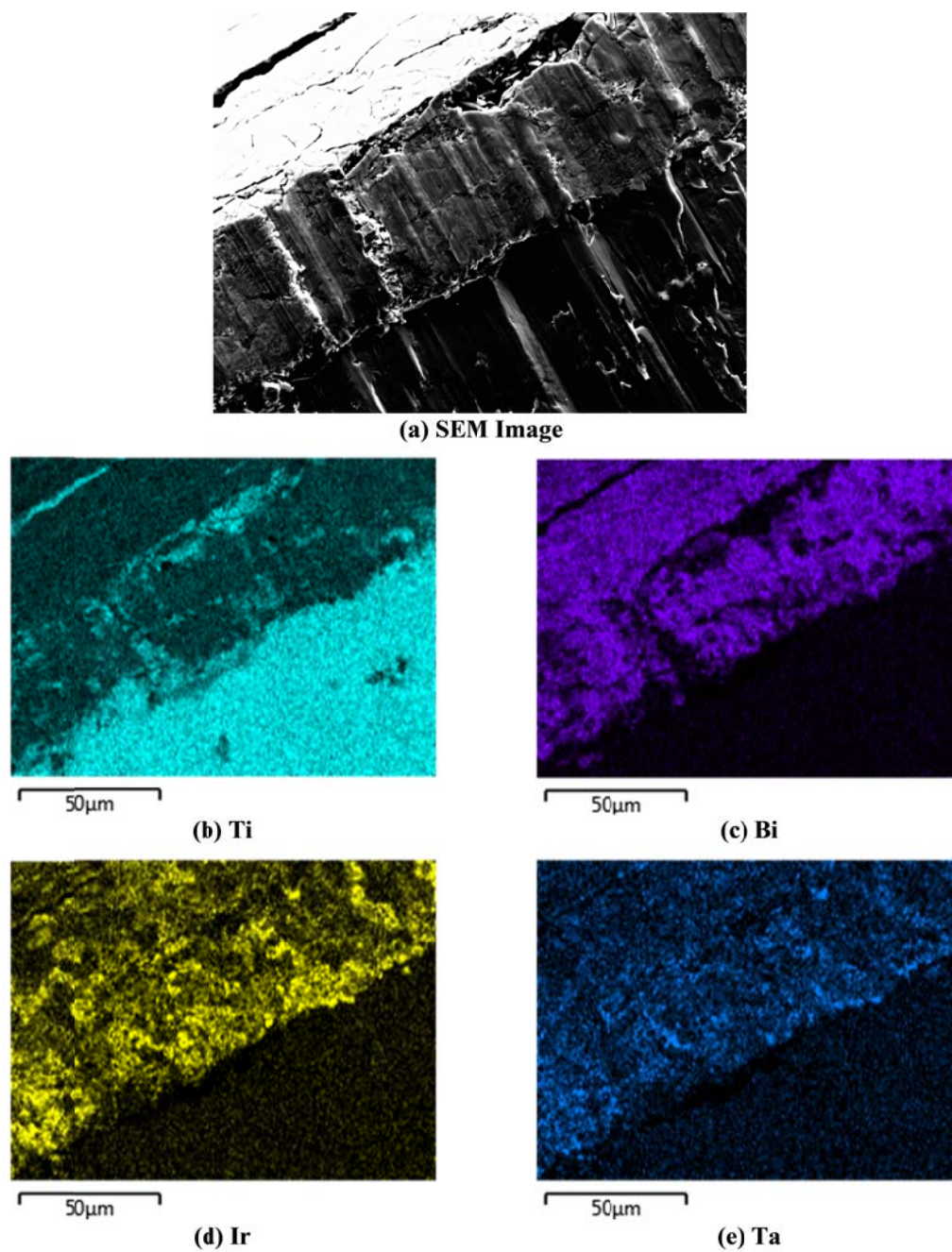


Figure 5.2. Scanning Electron Microscopy (SEM) image (a) of cross-section view for $\text{Ir}_{0.7}\text{Ta}_{0.3}\text{O}_y / \text{Bi}_{0.3}\text{Ti}_{0.7}\text{O}_z$ hetero-junction anode with Energy Dispersive Spectroscopy (EDS) mapping of Ti (b), Bi (c), Ir (d), and Ta (e).

undergoing the electrochemical experiments. The horizontal morphology of the outer surface appeared to have a cracked and fragmented shapes, where the size of discrete islands appeared to be the lowest for $x = 0.1$. Observations of vertical cross-section estimated the total depth of mixed metal oxides deposit on Ti support to be approximately 70 μm , while suggested that the depth of cracks is much less than the total film thickness. The surficial cracks were more distinct for the binary compositions ($x = 0.1 \sim 0.7$), which presumably ascribed to the differences in thermal expansion coefficients of titanium and bismuth oxides.¹⁰ The interface between the underlying $\text{Ir}_{0.7}\text{Ta}_{0.3}\text{O}_y$ and $\text{Bi}_x\text{Ti}_{1-x}\text{O}_z$ was not distinct perhaps due to inter-diffusions of ions. An EDS mapping image on a cross-section view of $\text{Ir}_{0.7}\text{Ta}_{0.3}\text{O}_y/\text{Bi}_{0.3}\text{Ti}_{0.7}\text{O}_z$ anode (Figure 5.2) indicated, in fact, that thermal inter-diffusion of the metal ions had taken place across the hetero-junction during annealing, on the basis of vertical gradients of Ir and Ta signals.

According to the XRD profiles (Figure 5.3), the hetero-junction anode without Bi doping ($x = 0$) was characterized by a mixture of anatase and rutile phase TiO_2 . In the presence of Bi with fractions higher than 10%, the peak from the anatase TiO_2 ($2\theta = 25^\circ$) disappeared. The anatase TiO_2 structure has been known to be transformed into a thermodynamically more stable rutile structure by thermal stresses with temperatures higher than 600 $^\circ\text{C}$.²⁹ However, evidence has been presented that an existence of impurities in the TiO_2 lattice structure can significantly reduce the transition temperature;¹ the annealing temperature in this study was 425 $^\circ\text{C}$, which is in the lower range reported by Hanaor and Sorrell²⁹. In addition, Tomita *et al.*²⁵ reported the crystalline structure of TiO_2 prepared from the aqueous titanium-glycolate complexes can

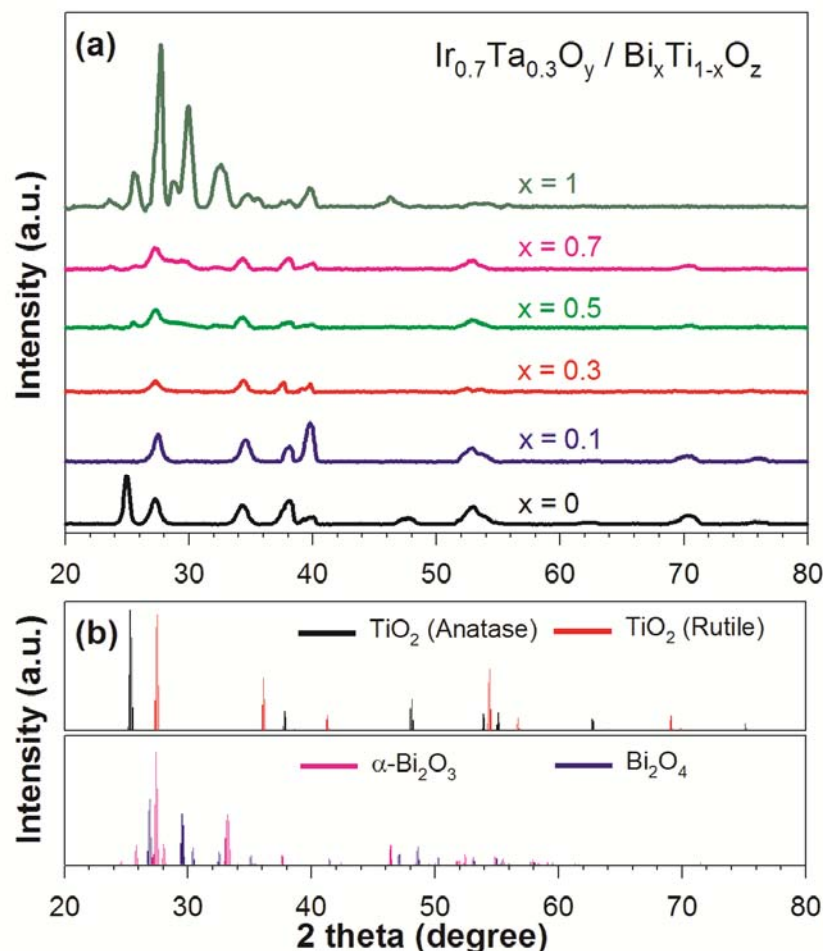


Figure 5.3. X-ray diffraction patterns of hetero-junction anodes $\text{Ir}_{0.7}\text{Ta}_{0.3}\text{O}_y / \text{Bi}_x\text{Ti}_{1-x}\text{O}_z$ with variable molar fraction (x) of Bi (a) referenced with a library for metal oxides of interests (b).

be influenced by the pH of precursor solution. With the current formulation for preparation of the anodes, the process of mixing with the Bi precursor (bismuth citrate dissolved in ammonia) should elevate the mixture precursor pH. In the absence of Ti ($\text{Ir}_{0.7}\text{Ta}_{0.3}\text{O}_y/\text{BiO}_z$), the surficial XRD patterns indicate α -phase Bi_2O_3 and Bi_2O_4 , suggesting that the effective oxidation state of Bi is a mixture of +3 and +5. In this regard, it is well known that monoclinic $\alpha\text{-Bi}_2\text{O}_3$ is converted to cubic $\delta\text{-Bi}_2\text{O}_3$ at temperatures

higher than 730 °C. After cooling the product, metastable β - and γ -phase Bi_2O_3 are found.²³ A visual observation, that the light yellow color of the initial composite as deposited changed into white after the electrochemical experiments, implied that the partial oxidation of Bi (III) to Bi (V) was likely to occur via an anodic potential bias rather than via thermal annealing. For the hetero-junction anodes with Bi fraction from 0.3 to 0.7, the diffraction intensities appeared to be much lower than the other compositional formulations using the same XRD instrument. The relative differences in the effective ionic radii of Bi (103 pm) and Ti (60.5 pm) may result in distortions in the lattice microstructure, which is often observed in binary metal oxide thin film.³⁰

The infrared absorption bands of the hetero-junction anodes in contact with deionized water (Figure 5.4a) were mostly characterized by broad bands at 3000 – 3600 cm^{-1} , relatively sharp peaks centered at 1640 cm^{-1} , and prominent bands starting at around 900 cm^{-1} . Peaks at 1640 cm^{-1} are usually assigned to bending (deformation) vibrations of free or physi-sorbed water, while the absorption bands ranged from 3000 to 3600 cm^{-1} are ascribed to stretching vibrations of surface titanol group ($>\text{Ti-OH}$) or hydrogen bonded H_2O . Absorption regions at wavenumbers lower than 900 cm^{-1} occur owing to fundamental vibrations of oxides lattice, particularly from M-O stretching and M-O-M bridging modes (where M is Ti or Bi). The minor peaks at around 2400 cm^{-1} are attributed to adsorption of carbonaceous species from air. Regarding the Bi-enriched hetero-junction anodes ($x = 0.7$ and 1), peaks centered near 1400 cm^{-1} appeared due to hydrated bismuth oxide moieties or surface hydroxyl functionalities (*i.e.*, $>\text{Bi-OH}$) via hydrolysis as in the common case of metal oxides exposed to water (*e.g.*, TiO_2 , Fe_2O_3 , SiO_2 , WO_3 , etc.). The absorption peaks near 3300 cm^{-1} broadened as the fraction of Bi

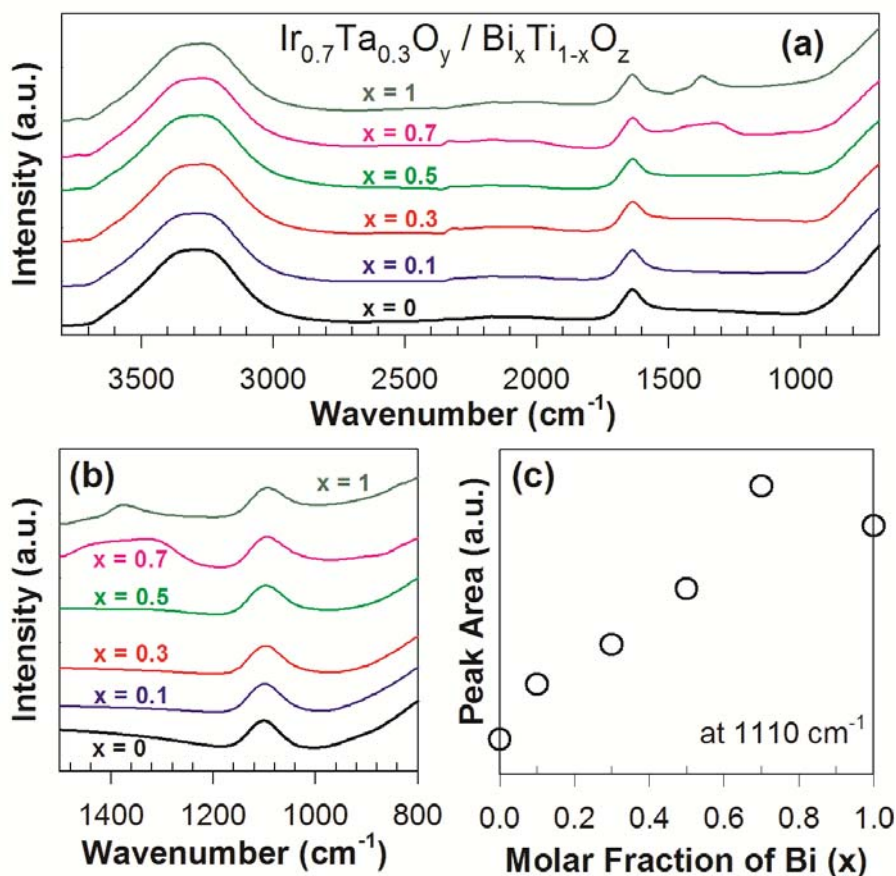


Figure 5.4. Fourier transform infrared spectroscopy with attenuated total reflectance (FTIR-ATR) analysis of $\text{Ir}_{0.73}\text{Ta}_{0.27}\text{O}_y/\text{Bi}_x\text{Ti}_{1-x}\text{O}_z$ hetero-junction anodes with variable molar fraction (x); (a) in contact with deionized water, (b) in contact with 1 M NaClO_4 solutions, (c) integrated intensities of peaks at 1110 cm^{-1} in contact with 1 M NaClO_4 solutions. Each adsorption spectra was collected with respect to the background signal of the contacting liquid.

increased. In contrast, the intensity of the peak at 1640 cm^{-1} did not change along with the molar fraction of Bi, presumably due to the interference of interstitial water molecule layers between solid samples and internal reflectance element. Evidence has been presented that the absorption bands in this range (1640 cm^{-1}) originate primarily from coordinated H_2O rather than from surficial hydroxyl group.³¹

According to traditional models describing the surface charge of metal oxides based on their amphoteric nature, the IR absorption from M-OH bonds is expected to decay with the deprotonation of OH functionalities. Therefore, increased isoelectric point of metal oxides at a given solution composition (bulk pH) would allow for losses in absorption by M-OH. In an attempt to assess the role of Bi on the surface charge more clearly, IR spectra were collected in 1 M NaClO₄ background solutions with circum-neutral pH. Aside from the absorption profiles described above, characteristic peaks of adsorbed ClO₄⁻ appeared at 1110 cm⁻¹ (Figure 5.4b). The integrated intensities of the characteristic peaks monotonically increased along with the molar fraction of Bi (Figure 5.4c). This observation clearly demonstrates that an increase in the surficial Bi fraction is accompanied by an increase in positive surface charges.

5.3.2. Voltammetric Characteristics. Water oxidation on metal oxide anodes is initiated by the one electron oxidation of surface hydroxyl groups to form bound hydroxyl radical (>MO_x(·OH)) and, sequentially, these intermediate states can be further oxidized to higher oxides (>MO_x).^{4,5,14} Eqs 5.2-5.5 describe the overall reaction sequence of the OER,^{17,32,33} where the rate constant for each reaction step is governed by the bond strength between the corresponding metal ion and active oxygen.^{15,16}

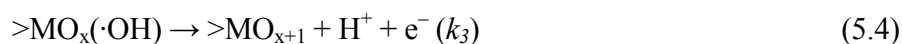
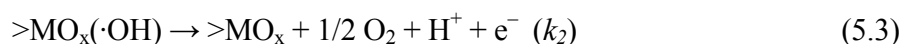
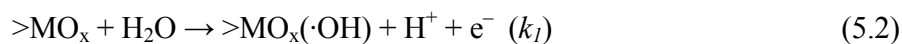


Figure 5.5a illustrates the electrochemical activities of the $\text{Ir}_{0.7}\text{Ta}_{0.3}\text{O}_y/\text{Bi}_x\text{Ti}_{1-x}\text{O}_z$ hetero-junction anodes in 50 mM NaCl solutions with circum-neutral pH in terms of current density (J) during anodic polarization. The anodic wave followed a quasi-linear relation with the applied potential; *i.e.*, an exponential dependence given by the Butler-Volmer formulation was relaxed due to an increase in ohmic resistance. The onset potential for the anodic current, which is defined as the iR -corrected anodic potential ($E_a - iR$) at the J of 1 A m^{-2} ,³⁴ was observed at near 1.2 V on average without a significant variation with composition (coefficient of variation: 5 %). The corresponding overpotential of OER was 0.4 V, which is comparable to previously reported values for anodes based on IrO_2 .^{7,33} The Tafel slopes, from the linear regions of $\log J$ versus $E_a - iR$ relationships, appeared to be near $120 \text{ mV decade}^{-1}$ in the range of $E_a - iR$ lower than 1.55 V. These values were not dependent on the surface composition as well (coefficient of variation: 7%). Under a larger anodic bias, there were substantial increases in the Tafel slopes most likely due to mass transport limitations. The observed Tafel slopes can be interpreted in terms of the initial formation of hydroxyl radical (eq 5.2) as the rate-determining step.^{15,17,32}

In the absence of the $\text{Ir}_{0.7}\text{Ta}_{0.3}\text{O}_y$ layer, the current generation was always negligible, as shown in Figure 5.5a ($\text{Bi}_{0.3}\text{Ti}_{0.7}\text{O}_z$ as an example). Even with the presumed redox transitions of surficial Bi, the $\text{Ir}_{0.7}\text{Ta}_{0.3}\text{O}_y$ layer was essential as an ohmic contact to overcome the Schottky barrier to electron transfer (metal oxides toward base metals). The magnitudes of J on the hetero-junction anodes were lower than on the $\text{Ir}_{0.7}\text{Ta}_{0.3}\text{O}_y$ anode, owing to the electrical resistance across the hetero-junction. In addition, the intensity of

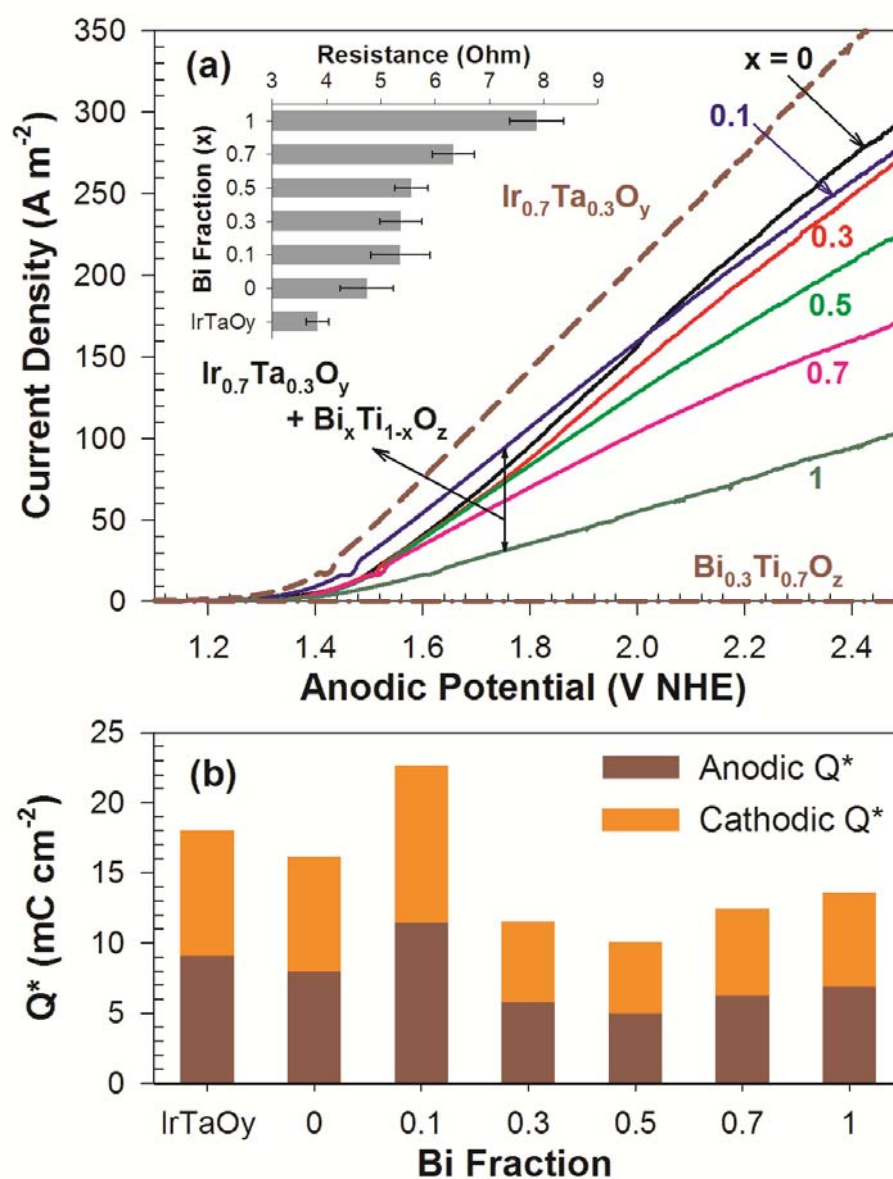


Figure 5.5. (a) Current generation during linear sweep voltammetry (scan rate: 5 mV sec^{-1}) together with (a, inset) ohmic resistance measured by current interruption and (b) integrated charge (Q^*) during cyclic voltammetry (scan range: $0.2 \sim 1.0 \text{ V NHE}$, scan rate: 20 mV sec^{-1}) with $\text{Ir}_{0.73}\text{Ta}_{0.27}\text{O}_y/\text{Bi}_x\text{Ti}_{1-x}\text{O}_z$ hetero-junction anodes with variable molar fraction (x); electrolyte: 50 mM NaCl ($\text{pH} \sim 7$), cathode: stainless steel, geometric surface area: $3 \times 2 \text{ cm}^2$. Data for $\text{Ir}_{0.7}\text{Ta}_{0.3}\text{O}_y$ or $\text{Bi}_{0.3}\text{Ti}_{0.7}\text{O}_z$ anode are shown as references.

the anodic wave decreased as the molar fraction of Bi increased. In light of nearly consistent onset potentials and Tafel slopes, the effects of Bi content on current generation can be explained in terms of the ohmic resistance measured by a current interruption technique (inset of Figure 5.5a). The ohmic resistance consists of electrolyte resistance to ion migration, polarization resistance coupled with resistance across the catalytic film.³⁵ Their combined effects can be depicted as resistors in series for a simplified equivalent (*e.g.*, Randles circuit).^{10,32,36-38} Because double layer capacitances usually overwhelm the physical capacitances of metal oxides films by several orders of magnitude,³⁷ the polarization resistance would not significantly contribute to the ohmic resistances in measurements by the current interruption method.³⁵ Therefore, the adverse effects of the Bi content on current response are ascribed to an increasing electrical resistance within the anode. This observation is therefore analogous to p-n junction under reverse bias, since the Bi_2O_3 has often been regarded as a p-type semiconductor.³⁹

On the other hand, integrated charge (Q^*) in a cyclic voltammogram within the potential region between the hydrogen evolution reaction and OER has been widely used as a parameter for electrochemically active surface area.^{8,10,36} Figure 5.6 shows the CV profiles in 50 mM NaCl solutions under E_a between 0.2 and 1.0 V. The integrated charges in anodic current (anodic Q^*) was superimposable to those in cathodic current (cathodic Q^*), as depicted in Figure 5.5b. The reversible redox reactions (described either by eq 5.2 or eq 5.4) at the active sites should account for the symmetric voltammograms.⁸ The ratio of Ti to Bi contents was not well correlated with the magnitude of Q^* , which was observed to be the highest for the Bi fraction of 0.1. In addition, there was little

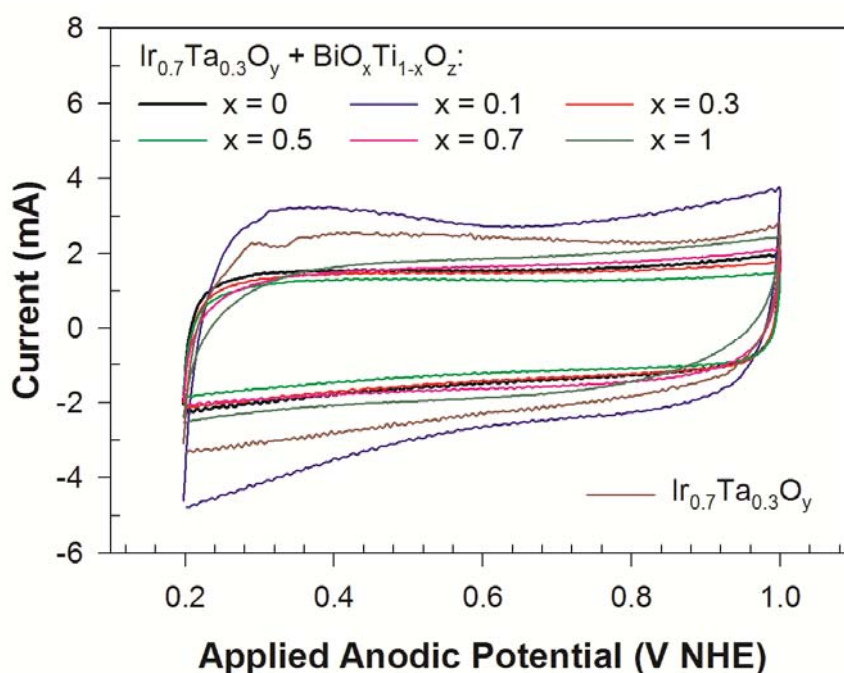


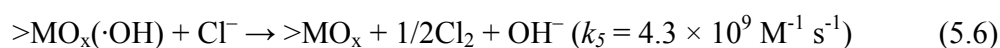
Figure 5.6. Cyclic voltammogram of $\text{Ir}_{0.7}\text{Ta}_{0.3}\text{O}_y/\text{Bi}_x\text{Ti}_{1-x}\text{O}_z$ hetero-junction anode with variable molar fraction of Bi (x) referenced with $\text{Ir}_{0.7}\text{Ta}_{0.3}\text{O}_y$ anode; counter electrode: stainless steel, geometric surface area: $3 \times 2 \text{ cm}^2$, electrolyte: 50 mM NaCl, scan range: 0.2 – 1.0 V NHE, scan rate: 20 mV sec^{-1} .

relationship between the current density and Q^* , which suggests that the current generation is primarily governed by ohmic resistance rather than by the surface area.

5.3.3. Reactive Chlorine Species Generation. Figure 5.7 shows reactive chlorine generation on $\text{Ir}_{0.7}\text{Ta}_{0.3}\text{O}_y/\text{Bi}_x\text{Ti}_{1-x}\text{O}_z$ hetero-junction anodes in 50 mM NaCl solutions. The E_a was adjusted from 2.0 to 3.0 V, which corresponded to the cell voltage from 4 to 6 V versus the counter electrode. The current generation during the course of potentiostatic electrolysis (Figure 5.7a) was in general agreement with the polarization curve in Figure 5.5a. In comparison with the $\text{Ir}_{0.7}\text{Ta}_{0.3}\text{O}_y$ anode, the quasi-steady-state values of J were reduced for the hetero-junction anodes by 20 to 60% as the molar

fraction of Bi increased, primarily due to augmented iR (*vide supra*). Nevertheless, the $\text{Bi}_x\text{Ti}_{1-x}\text{O}_z$ hetero-junction layer was found to substantially increase the current efficiency of RCS generation as calculated using eq 5.1 (Figure 5.7c). The η_{RCS} was estimated to average 53% for $\text{Ir}_{0.7}\text{Ta}_{0.3}\text{O}_y$ anode, in agreement with previous reports under comparable condition.²⁸ This value increased to 85% via the layering of a protective overcoat of TiO_2 ($x = 0$). Even higher magnitudes of η_{RCS} were observed for the hetero-junction anodes with Bi contents of 10 or 30%. Consequently, the rates of RCS generation (Figure 5.7b) were enhanced by a factor of 20 to 30%. The improvements in η_{RCS} should be underscored because the energy efficiency, in terms of the specific RCS generation rate normalized by power input, is directly proportional to the η_{RCS} (and cell voltage).

The electrochemical oxidation of chloride ion on metal oxides anodes occurs due to reactions with either hydroxyl radical or active oxygen adsorbed on the surface, as described by the following equations:^{5,13,40}



Outer-sphere electron transfer from chloride ion (eq 5.6) is most likely much faster than by direct transfer of active surficial oxygen (eq 5.7). In this regard, the η_{RCS} is likely to be determined primarily by speciation between $>\text{MO}_x(\cdot\text{OH})$ and $>\text{MO}_{x+1}$. The relative concentration of surface reactive oxygen will depend on the rate of eq 5.4, whose electro-stationary distribution can be described in terms of a ‘Nernstian’ equilibrium. The

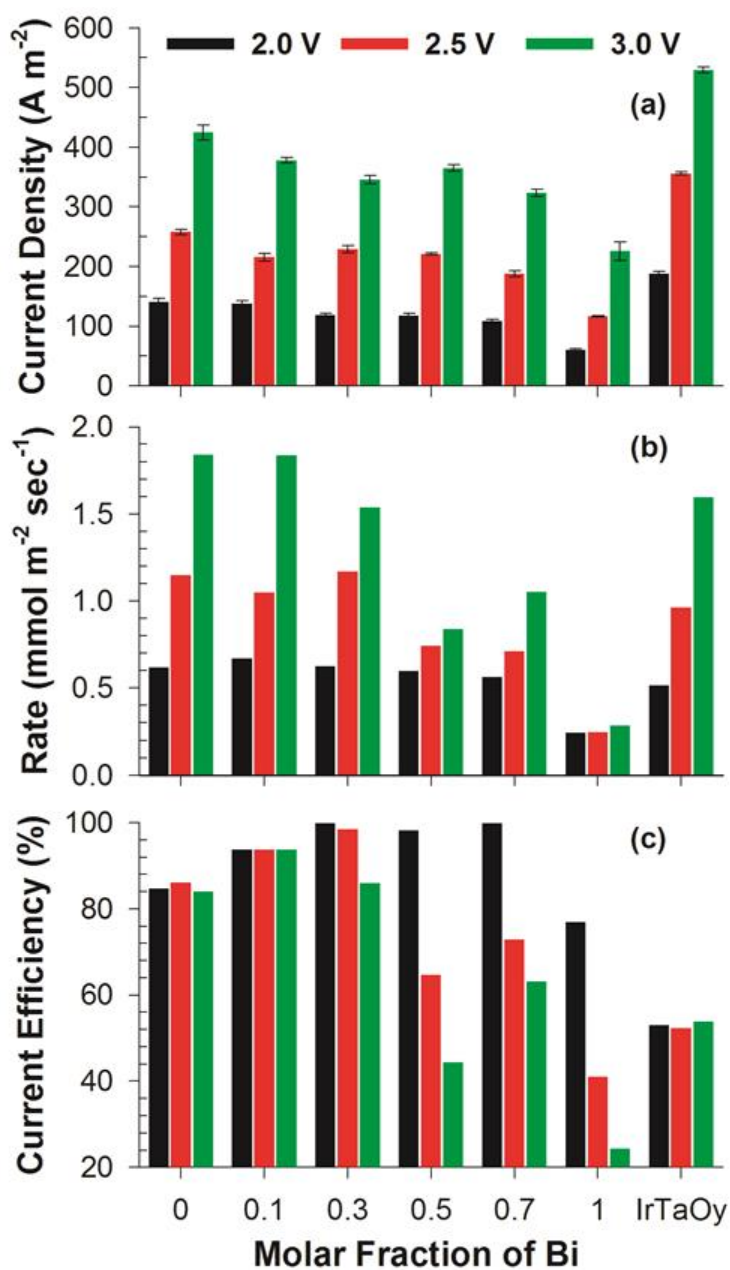


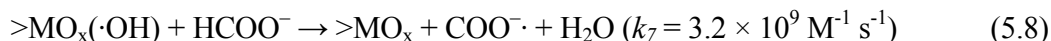
Figure 5.7. (a) Mean current density together with (b) specific rate and (c) current efficiency of reactive chlorine species generation during the course of potentiostatic electrolysis with $Ir_{0.7}Ta_{0.3}O_y/Bi_xTi_{1-x}O_z$ hetero-junction anodes with variable molar fraction (x); electrolyte: 50 mM NaCl (pH \sim 7), cathode: stainless steel, geometric surface area: $3 \times 2\ cm^2$, applied anodic potential: 2.0, 2.5, 3.0 V NHE. Data for $Ir_{0.7}Ta_{0.3}O_y$ anode are shown as references.

increase in η_{RCS} on $\text{Bi}_x\text{Ti}_{1-x}\text{O}_z$ hetero-junction system can be explained as the lower to higher oxide transition via electron transfer is more thermodynamically favorable (*i.e.*, lower enthalpy change) to IrO_2 rather than to TiO_2 .

When Bi is the majority surface constituent ($x = 0.5$ to 1), the η_{RCS} decreased with increasing anodic potential. The decrease of η_{RCS} could be possibly explained in association with bulk pH. Electrolysis in dilute NaCl solutions results in an increase of pH from non-stoichiometric water splitting.⁴¹ The increase of solution pH that is proportional to the conversion of chloride ion to RCS favors the OER since higher pH reduces the redox potential of water oxidation. In some cases, however, the Bi may accelerate the higher oxide formation²⁴ with a net result of increasing rate with increasing anodic potential.

5.3.4. Formate Ion Degradation. Formate ion was used in this study as a prove for surface-bound hydroxyl radical.²⁰ Many investigators employ reactive dye compounds such as methylene blue and RNO (p-nitrosodimethylaniline) for quantitative $\cdot\text{OH}$ estimation with relatively simple instrumentation.^{14,42} However, the low aqueous solubility of these dye compounds limits the operational concentration (< 1 mM). Furthermore, degradation of a dye compound via a direct electron transfer or active oxygen transfer from higher oxides has been reported for IrO_2 -based anodes.⁴² The reaction between formate ion and $\cdot\text{OH}$ produces the carbon dioxide radical anions (eq 5.8 and 5.9) and the homogeneous bimolecular rate constants for this sequence are well known.⁴³ We assume that oxygen atom transfer from $>\text{MO}_{x+1}$ to formate is very slow in

comparison. For example, the O-atom transfer between ozone and formate ion was reported to be in the range of $10^2 \text{ M}^{-1} \text{ s}^{-1}$.⁴³



$$[>\text{MO}_x(\cdot\text{OH})]_{\text{ss}} = \frac{k_{\text{formate}}^{\text{obs}} (\text{s}^{-1})}{3.2 \times 10^9 \text{ M}^{-1} \text{ s}^{-1}} \quad (5.10)$$

The formate ion degradation in 50 mM NaCOOH solutions (Figure 5.8) followed pseudo-first-order reaction profile that in turn allows for a steady-state kinetic analysis. The quasi-steady-state concentration of hydroxyl radical on each anode surface ($[>\text{MO}_x(\cdot\text{OH})]_{\text{ss}}$) was estimated according to the observed pseudo-first-order rate constant of formate decay ($k_{\text{formate}}^{\text{obs}}$), using eq 5.10, given the homogeneous bimolecular rate constant. The estimated concentration of $>\text{MO}_x(\cdot\text{OH})$ (Figure 5.9) was orders of magnitude lower than the typical site density of $>\text{Ti-OH}$ moieties on TiO_2 particles ($1 \times 10^{-8} \text{ mol cm}^{-2}$), but in comparable order with estimations for thin film TiO_2 electrodes.⁴¹

The rates of formate degradation rate under variable surface composition (Figure 5.9) were largely in parallel with those of RCS generation; both the $k_{\text{formate}}^{\text{obs}}$ and $[>\text{MO}_x(\cdot\text{OH})]_{\text{ss}}$ showed peaks at x of 0.1 or 0.3 and monotonically decreased with further increases of the Bi content. This observation could also result from a combinational consequences of ohmic resistance (*vide supra*) and branching ratio of $>\text{MO}_x(\cdot\text{OH})$ to $>\text{MO}_{x+1}$. However, in comparison with the hetero-junction anodes giving the highest rate

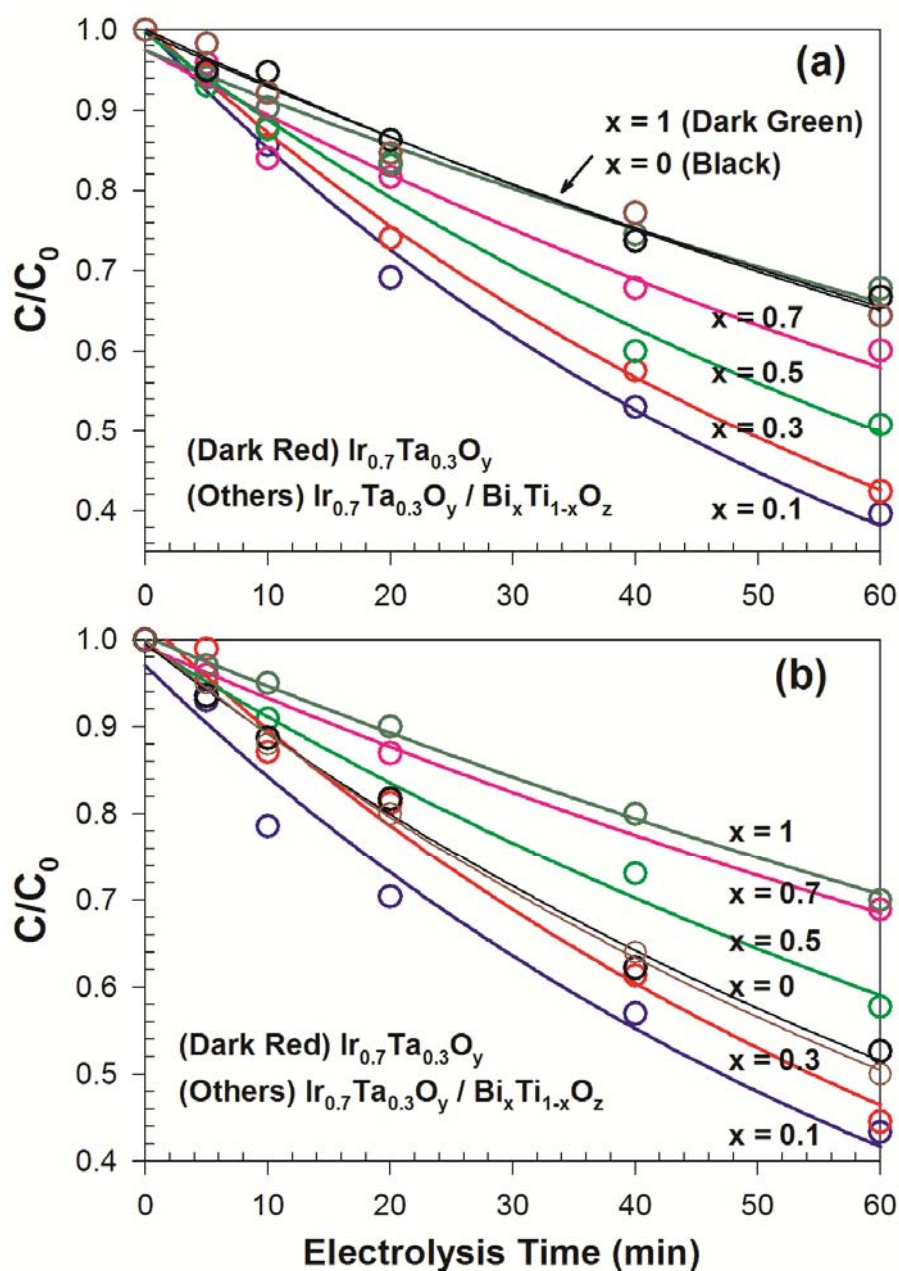


Figure 5.8. Time profiles of formate ion oxidation during the course of potentiostatic electrolysis with $\text{Ir}_{0.7}\text{Ta}_{0.3}\text{O}_y/\text{Bi}_x\text{Ti}_{1-x}\text{O}_z$ hetero-junction anodes with variable molar fraction (x); electrolyte: 50 mM NaCOOH , cathode: stainless steel, geometric surface area: $3 \times 2 \text{ cm}^2$, applied anodic potential: (a) 2.5 and (b) 3.0 V NHE. Data for $\text{Ir}_{0.7}\text{Ta}_{0.3}\text{O}_y$ anode are shown as references.

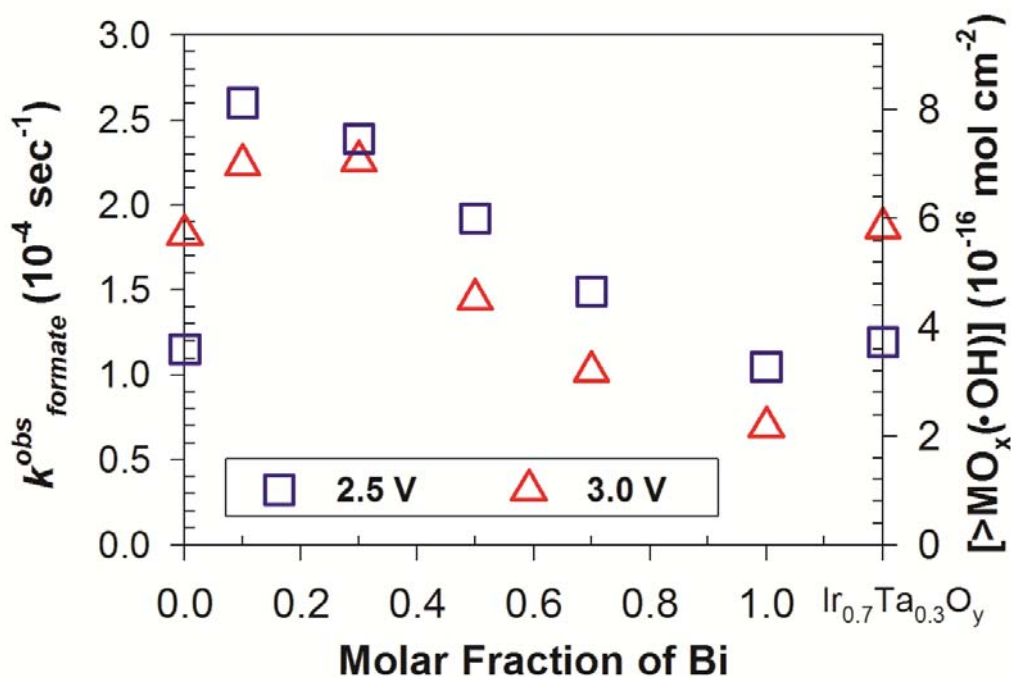


Figure 5.9. Observed pseudo-first-order rate constant of formate ion oxidation with corresponding surface hydroxyl radical concentration during the course of potentiostatic electrolysis with $\text{Ir}_{0.7}\text{Ta}_{0.3}\text{O}_y/\text{Bi}_x\text{Ti}_{1-x}\text{O}_z$ hetero-junction anodes with variable molar fraction (x); electrolyte: 50 mM NaCOOH, cathode: stainless steel, geometric surface area: $3 \times 2 \text{ cm}^2$, applied anodic potential: 2.5 or 3.0 V NHE. Data for $\text{Ir}_{0.7}\text{Ta}_{0.3}\text{O}_y$ anode are shown as references.

constants ($x = 0.1$ or 0.3), the anodes without Bi ($\text{Ir}_{0.7}\text{Ta}_{0.3}\text{O}_y$ with or without TiO_2 hetero-junction) resulted in slower reactions with HCOO^- (particularly at the E_a of 2.5 V). Recalling that the anodes without Bi showed comparable RCS generation rates with the hetero-junction anodes with x of 0.1 or 0.3, contributions of lattice oxygen atoms to RCS generation appear to be more significant for anodes without Bi. On the other hand, when Bi fraction exceeds 0.1, the $[>\text{MO}_x(\cdot\text{OH})]_{\text{ss}}$ at the E_a of 3.0 V was found to be even lower than those at 2.5 V.

5.3.5. Stability. The accelerated life tests are the most widely used protocols to estimate the service life of anodes for OER or CIER. In these methods, the goal is usually to monitor the cell voltage under a harsh galvanostatic environment (J up to 1 A cm^{-2}) such that the dissolution or detachment of electro-active catalysts occurs more rapidly. An accelerated life, as determined by the point when an abrupt jump of cell voltage occurs along with complete deactivation, can be converted into an estimated service life under practical operating conditions according to empirical proportionalities to $J^{1/m}$ (m range from 1.4 to 2.0).¹¹ However, in the case of the hetero-junction anodes, removal of the outer $\text{Bi}_x\text{Ti}_{1-x}\text{O}_z$ layer would not deteriorate the voltammetric response from the $\text{Ir}_{0.7}\text{Ta}_{0.3}\text{O}_y$ layer. In this regard, the definition of accelerated life was modified to an endpoint in which the free metal concentration in the background electrolyte would signify complete failure of $\text{Bi}_x\text{Ti}_{1-x}\text{O}_z$ layer. Passivation of the base metal by insulating TiO_2 ¹¹ was assumed to be insignificant when compared to dissolution or detachment of the catalytic films.

Figure 5.10 shows the variations of cell voltage and cumulative metal concentrations in the electrolyte (1 M NaClO_4 solutions) during the course of galvanostatic electrolysis. The electrolyte solution was maintained to have near circum-neutral pH. During the life test, the cell voltage ranged from 4.0 to 5.5 V (Figure 5.10a) without a noticeable failure for 48 h of electrolysis. The impact of an increasing ohmic resistance for higher Bi levels was not obvious because of fluctuations in cell voltage that were associated with vigorous bubble generation and changes in electrode area exposed to solutions. The dissociation of the $\text{Bi}_x\text{Ti}_{1-x}\text{O}_z$ layer is likely to be via dissolution rather than detachment since macro-

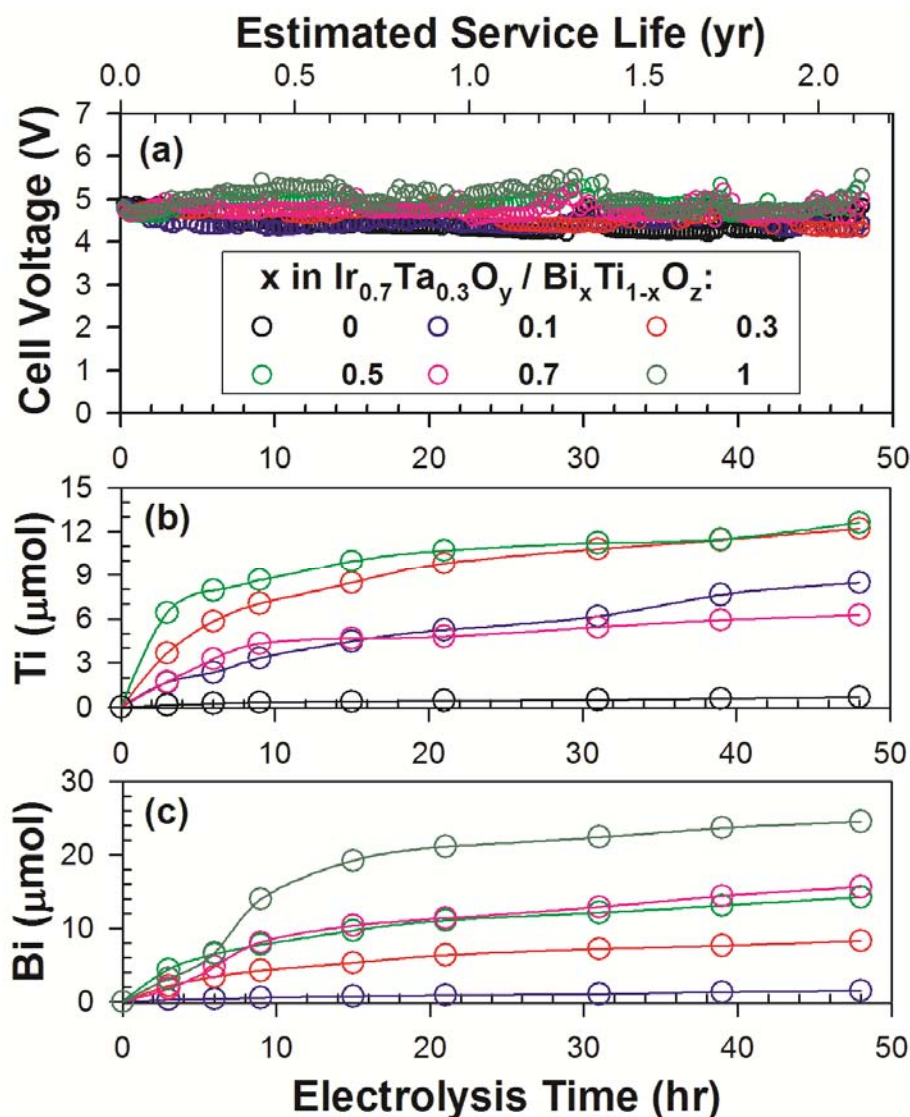


Figure 5.10. Variations of cell voltage (a) together with cumulative molar amounts of dissociated Ti (b) and Bi (c) during the course of galvanostatic electrolysis with $\text{Ir}_{0.7}\text{Ta}_{0.3}\text{O}_y/\text{Bi}_x\text{Ti}_{1-x}\text{O}_z$ hetero-junction anodes with variable molar fraction (x); electrolyte: 1 M NaClO_4 (pH ~ 7), cathode: stainless steel, geometric surface area: $2 \times 0.5 \text{ cm}^2$, current density: 1 A cm^{-2} . Estimated service life under operating current density of 300 A m^{-2} is shown in a parallel axis with electrolysis time (h) with proportionality to current density^{1/1.7}.

particles did not exist in visual observations of the electrolyte. The cumulative amounts of dissolved Bi (Figure 5.10c) increased faster with augmenting Bi content, which indicates that Bi components mitigate the stability of the $\text{Bi}_x\text{Ti}_{1-x}\text{O}_z$ layer. According to the Pourbaix diagram of Bi,⁴⁴ the vicinal acidity produced by water discharge should be responsible for the dissolution of Bi_2O_3 to Bi(III) ions (Bi^{3+} , BiOH^{2+} , BiO^+), whereas higher oxides of Bi (Bi_4O_7 , Bi_2O_4 , and Bi_2O_5) are expected to require more acidic pH for dissolution. Destruction of the Ti lattice appeared to accompany the dissolution of Bi, as illustrated by the cumulative Ti concentration in Figure 5.10b. The highest amount of Ti released into the solution was observed for an anode with an equi-molar ratio of Ti to Bi ($x = 0.5$).

5.4. DISCUSSION

From an analogy with Hume-Rothery rules, Bi_2O_3 was not expected to constitute a homogeneous solid solution within the TiO_2 lattice, because of substantial differences in lattice structure (tetragonal for rutile TiO_2 ¹⁹ and monoclinic for α -phase Bi_2O_3 ^{23,45}) and effective radius of metal ions. In addition, the XRD intensity profiles of $\text{Ir}_{0.7}\text{Ta}_{0.3}\text{O}_y/\text{Bi}_x\text{Ti}_{1-x}\text{O}_z$ anodes showed insignificant variations with respect to the fraction of Bi. Therefore, the microstructure of the outer layer is likely to be a mixed phase oxide crystal with a limited miscibility.^{6,38} Given this assumption, the physico-chemical characteristics of the $\text{Bi}_x\text{Ti}_{1-x}\text{O}_z$ layer should locally conform to the properties of TiO_2 and Bi_2O_3 individually for which the overall characteristics would depend on the molar mixing ratio. For example, the instability of Bi under (water discharge induced) acidic condition agrees with the phase transformation given by Pourbaix diagram of Bi_2O_3 .⁴⁴

The electrochemically active surface areas estimated by Q^* were found to be primarily determined by physical surface area. As shown in Figure 5.11, the Q^* of the anodes under investigation (Figure 5.5b) followed fairly well an inverse relationship with the physical lattice dimensions estimated by the XRD peaks in Figure 5.3 and the Scherrer equation. Regardless of the type of metal ions, the hydrous metal oxides can serve as electrochemically active sites as long as proper electron shuttles are electrically accessible.³⁰ This correlation in spite of the variation in surface composition indicates that the $\text{Ir}_{0.7}\text{Ta}_{0.3}\text{O}_y$ layer is the acting electron carrier in this potential window (0.2 to 1.0 V).^{8,10} The half potentials of the symmetric voltamograms in Figure 5.6 were close to the redox potential of the $\text{Ir}_2\text{O}_3/\text{IrO}_2$ couple ($E = 0.51$ V, at pH 7). On a thermodynamic basis, the redox transitions of $\text{Ti}_2\text{O}_3/\text{TiO}_2$ ($E = -0.47$ V at pH 7) or $\text{Bi}/\text{Bi}_2\text{O}_3$ ($E = -0.04$ V at pH 7) are infeasible to drive the oxidation of surface hydroxyl group.

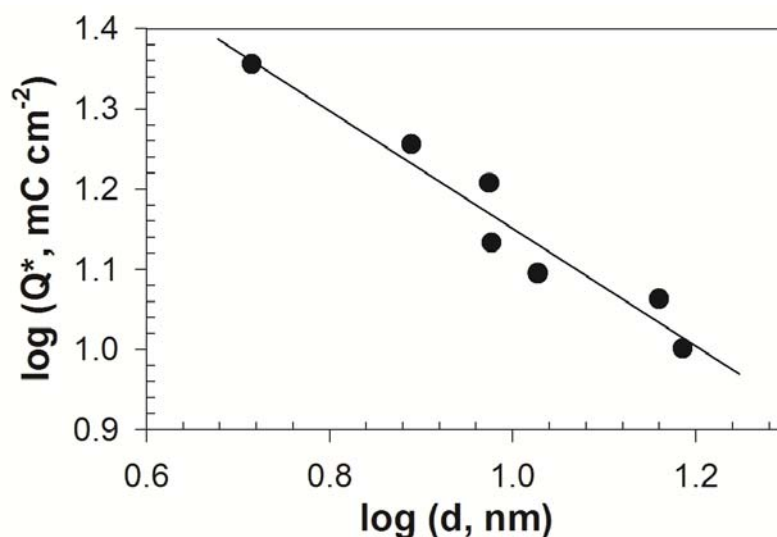


Figure 5.11. Relationship between Q^* as a parameter of electrochemically active surface area and crystalline dimension estimated from XRD intensity by Scherrer equation.

Moderate increases of η_{RCS} and $k_{formate}^{obs}$ with an increasing Bi fraction up to 0.3 should be primarily associated with the surface charge depending on the amphoteric properties of the metal oxides. The point of zero charge (pH_{pzc}) of Bi_2O_3 (9.4) is reported to be much greater than TiO_2 (5.1 – 6.4) or IrO_2 (3.3).⁴⁶ Thus, the surface of $Bi_xTi_{1-x}O_z$ layers should be more positively charged at higher Bi fraction, x . This change enhances the accumulation of anions (Cl^- and $HCOO^-$) in the electrical double layer. The magnitude of ClO_4^- adsorption in Figure 5.4c is consistent with this interpretation, given the monotonic increase in the characteristic IR peak area of ClO_4^- (at 1110 cm^{-1}) with the increase of x . In addition, Bi-doping increases the intensities of the Ti-OH bond under the molar fraction of Bi lower than 10%.^{47,48} Alves *et al.*⁹ also noted that substitution of TiO_2 with CeO_2 ($pH_{pzc} \sim 8.1$) increases the surface OH group concentration as measured by X-ray photoelectron spectroscopy. Stronger speciation of the -OH functionality towards protonated moieties, with corresponding IR signals either of $>Ti-OH$ ($3000\text{ to }3600\text{ cm}^{-1}$) or $>Bi-OH$ (centered at 1400 cm^{-1}), would be beneficial to the hydroxyl radical formation. The electro-stationary $[>MO_x(\cdot OH)]$ was estimated to be the highest for x of 0.1 or 0.3 (Figure 5.9), even though $[>MO_x(\cdot OH)]_{ss}$ should implicitly include the partitioning constants of formate ion in our simple kinetic analysis.

Under a potential bias within the domain of water splitting, the $>MO_x(\cdot OH)$ site should be quenched by a redox transformation of transition metal (Ir or Bi) to produce $>MO_{x+1}$. Given several simplifying assumptions for the kinetics of formate degradation, the rate constants for eq 5.4 (k_3) could be estimated by rearrangement of the governing equation for $[>MO_{x+1}]$ under pseudo-steady-state conditions.

$$k_3 = \frac{k_4[>MO_{x+1}]}{[>MO_x(\cdot OH)]_{SS}} = \frac{\eta_{O_2} I}{2F} \times \frac{1}{A[>MO_x(\cdot OH)]_{SS}} \quad (5.11)$$

where, η_{O_2} is the current efficiency of OER and A is the geometric surface area of the electrode. The η_{O_2} can be calculated from the charge balance equations. We also assume that $>MO_x(\cdot OH)$ and $>MO_{x+1}$ are exclusively responsible to $HCOO^-$ oxidation and OER, respectively; *i.e.*, eq 5.3 is relatively slow and productions of homogeneous reactive oxygen species (*e.g.*, H_2O_2 , O_3 , $O_2^{\cdot -}$) are negligible.

Figure 5.12 illustrates k_3 for $Ir_{0.7}Ta_{0.3}O_y/Bi_xTi_{1-x}O_z$ anodes which mostly increases together with the surficial Bi concentration. This finding suggests an oxidation of Bi(III) to Bi(IV) or Bi(V) can be an active electron sink for insertion of oxygen into the lattice. The behavior of Bi_2O_3 is analogous to that of electroactive IrO_2 , since Zhang *et al.*³³ reported that an increasing Ir fraction in $Ir_xSi_{1-x}O_y$ anodes nonlinearly promotes the rate constant of higher oxide formation. The redox potential at pH 7 is 0.92 V for Bi_4O_7/Bi_2O_3 and 1.13 V for Bi_2O_4/Bi_4O_7 couple. The Bi(V) would reduce the kinetic barrier to oxide transition more effectively, as supported by the considerable increase of k_3 with E_a (2.5 V versus 3.0 V). On the contrary, in the absence of surficial Bi, the influence of E_a on k_3 value was not distinct, raising a possibility that dismutations of bound hydroxyl radical ($2>MO_x(\cdot OH) \rightarrow >MO_x + >MO_{x+1} + H_2O$)^{8,17,49} might account for the higher oxides formation with Ir(IV)/Ir(VI) transition. The highest k_3 value was observed mostly for the $Ir_{0.7}Ta_{0.3}O_y$ layer, as expected by the redox potential of IrO_3/IrO_2 couple (0.94 V at pH 7) falling below that of Bi_2O_4/Bi_4O_7 couple. The kinetics of $>MO_x/>MO_{x+1}$ transition would

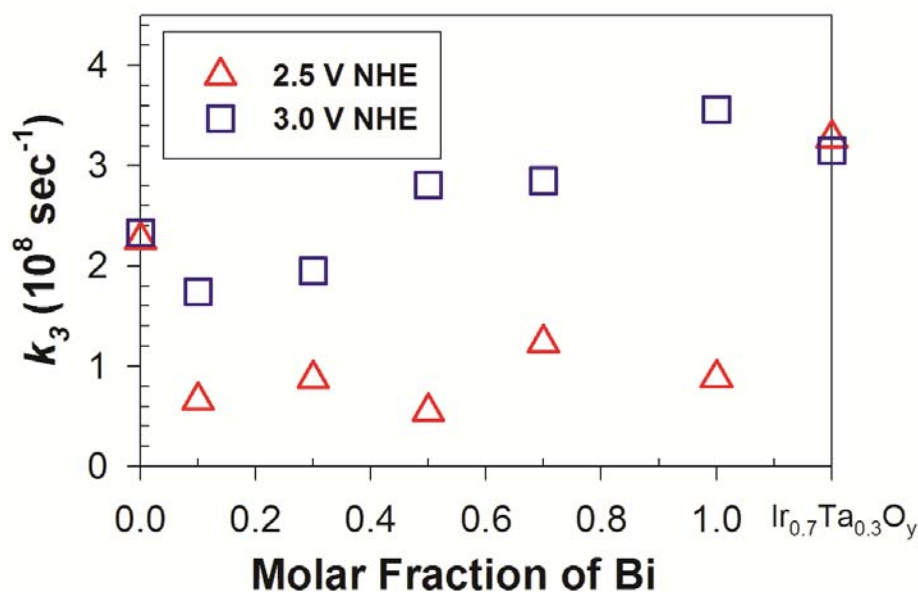


Figure 5.12. Estimated rate constant for transition from surface bound hydroxyl radical to higher oxide in 50 mM NaCOOH solutions.

also be influenced by concentrations of oxide ion vacancy in the lattice structure.¹⁴ The magnitudes of k_3 estimated in this study ($0.5 - 3.5 \times 10^8 \text{ sec}^{-1}$) were in a similar order with $k_3[\text{Cl}^-]$ ($2.2 \times 10^8 \text{ sec}^{-1}$) or $k_7[\text{HCOO}^-]$ ($1.6 \times 10^8 \text{ sec}^{-1}$). The relative reaction rate of [$>\text{MO}_x(\text{-OH})$] to form $>\text{MO}_{x+1}$ in comparison with oxidizing electron donating substrates (Cl^- or HCOO^-) would be the primary determinant of the current efficiency, which was found to be affected by the surface compositions and E_a . The higher oxide formation driven by electro-active Bi would rationalize the behaviors of anodes with high Bi contents ($x > 0.5$); the decrease of η_{RCS} and $k_{\text{formate}}^{\text{obs}}$ along with x and E_a .

The dissociation of $\text{Bi}_x\text{Ti}_{1-x}\text{O}_z$ layers would provoke a direct contact of the $\text{Ir}_{0.7}\text{Ta}_{0.3}\text{O}_y$ layer with the electrolyte and losses of Ir component, albeit the Ir concentrations in the electrolyte were always near the detection limit. Visual observation

of blackish deposits as well as EDS analysis confirmed precipitation of Ir, presumably in the form of $\text{Ir}(\text{OH})_x$, on cathodes. Compared with the estimated total metal loading (*ca.* 25 μmol), the hetero-junction anodes with Bi fractions higher than 0.5 approached complete dissociation after 21 h of electrolysis. The corresponding service life was estimated to be *ca.* 1 year assuming operational current density and the factor of m to be 300 A m^{-2} and 1.7, respectively. For the other anodes with lower Bi concentrations ($x = 0.1$ and 0.3), the cumulative metal concentrations in the electrolyte did not reach their expected plateaus, indicating service lives higher than 2 years. More importantly, the Ti concentration in electrolyte was negligible for $\text{Ir}_{0.7}\text{Ta}_{0.3}\text{O}_y/\text{TiO}_2$ anode throughout the experiments, demonstrating an outstanding stability in anodic environment. Even after the failure of the outer layer of the hetero-junction anodes, they can be regenerated with minimal cost by subsequent coating with oxide of earth-abundant and environmentally benign^{19,45} Ti and Bi.

In conclusion, we demonstrated that surface modification of an $\text{Ir}_{0.7}\text{Ta}_{0.3}\text{O}_y$ anode with an over layer of $\text{Bi}_x\text{Ti}_{1-x}\text{O}_z$ leads to an enhancement in current efficiency for reactive chlorine generation during the electrochemical oxidation of chloride ion. In particular, lower mole fractions of Bi in the surface layer ($x = 0 - 0.3$) yield higher current efficiency. Long-term operation can be achieved without the loss of Ir since the overlying $\text{Bi}_x\text{Ti}_{1-x}\text{O}_z$ layer prevents the $\text{Ir}_{0.7}\text{Ta}_{0.3}\text{O}_y$ from direct contact with electrolyte, even though bismuth oxide is vulnerable to dissolution under anodic environment. Results of this study could lead to improvements in commercial electrochemical chlorine production or to advanced treatment of high-salinity wastewater treatment with a reduced energy input.

5.5. REFERENCES

- (1) Menzel, N.; Ortel, E.; Mette, K.; Kraehnert, R.; Strasser, P. Dimensionally stable Ru/Ir/TiO₂-anodes with tailored mesoporosity for efficient electrochemical chlorine evolution. *Acs Catalysis* **2013**, *3* (6), 1324-1333.
- (2) Hu, W.; Wang, Y. Q.; Hu, X. H.; Zhou, Y. Q.; Chen, S. L. Three-dimensional ordered macroporous IrO₂ as electrocatalyst for oxygen evolution reaction in acidic medium. *Journal of Materials Chemistry* **2012**, *22* (13), 6010-6016.
- (3) Mamaca, N.; Mayousse, E.; Arrii-Clacens, S.; Napporn, T. W.; Servat, K.; Guillet, N.; Kokoh, K. B. Electrochemical activity of ruthenium and iridium based catalysts for oxygen evolution reaction. *Applied Catalysis B-Environmental* **2012**, *111*, 376-380.
- (4) Panizza, M.; Cerisola, G. Direct and mediated anodic oxidation of organic pollutants. *Chemical Reviews* **2009**, *109* (12), 6541-6569.
- (5) Martinez-Huitle, C. A.; Ferro, S. Electrochemical oxidation of organic pollutants for the wastewater treatment: direct and indirect processes. *Chemical Society Reviews* **2006**, *35* (12), 1324-1340.
- (6) Comminellis, C.; Vercesi, G. P. Characterization of DSA-type oxygen evolving electrodes - Choice of a coating. *Journal of Applied Electrochemistry* **1991**, *21* (4), 335-345.
- (7) Lee, Y.; Suntivich, J.; May, K. J.; Perry, E. E.; Shao-Horn, Y. Synthesis and activities of rutile IrO₂ and RuO₂ nanoparticles for oxygen evolution in acid and alkaline solutions. *Journal of Physical Chemistry Letters* **2012**, *3* (3), 399-404.
- (8) Alves, V. A.; Dasilva, L. A.; Boodts, J. F. C.; Trasatti, S. Kinetics and mechanism of oxygen evolution on IrO₂-based electrodes containing Ti and Ce acidic solutions. *Electrochimica Acta* **1994**, *39* (11-12), 1585-1589.
- (9) Alves, V. A.; da Silva, L. A.; de Castro, S. C.; Boodts, J. F. C. Surface characterization by UHV techniques and cyclic voltammetry of thermal IrO₂-based electrocatalysts containing TiO₂ and CeO₂. *Journal of the Chemical Society-Faraday Transactions* **1998**, *94* (5), 711-717.

- (10) daSilva, L. A.; Alves, V. A.; daSilva, M. A. P.; Trasatti, S.; Boodts, J. F. C. Oxygen evolution in acid solution on IrO₂+TiO₂ ceramic films. A study by impedance, voltammetry and SEM. *Electrochimica Acta* **1997**, *42* (2), 271-281.
- (11) Chen, X. M.; Chen, G. H.; Yue, P. L. Stable Ti/IrO_x-Sb₂O₅-SnO₂ anode for O₂ evolution with low Ir content. *Journal of Physical Chemistry B* **2001**, *105* (20), 4623-4628.
- (12) Chen, S. Y.; Zheng, Y. H.; Wang, S. W.; Chen, X. M. Ti/RuO₂-Sb₂O₅-SnO₂ electrodes for chlorine evolution from seawater. *Chemical Engineering Journal* **2011**, *172* (1), 47-51.
- (13) Hansen, H. A.; Man, I. C.; Studt, F.; Abild-Pedersen, F.; Bligaard, T.; Rossmeisl, J. Electrochemical chlorine evolution at rutile oxide (110) surfaces. *Physical Chemistry Chemical Physics* **2010**, *12* (1), 283-290.
- (14) Comninellis, C. Electrocatalysis in the Electrochemical conversion/combustion of organic pollutants for waste-water treatment. *Electrochimica Acta* **1994**, *39* (11-12), 1857-1862.
- (15) Trasatti, S. Electrocatalysis in the anodic evolution of oxygen and chlorine. *Electrochimica Acta* **1984**, *29* (11), 1503-1512.
- (16) Rossmeisl, J.; Qu, Z. W.; Zhu, H.; Kroes, G. J.; Norskov, J. K. Electrolysis of water on oxide surfaces. *Journal of Electroanalytical Chemistry* **2007**, *607* (1-2), 83-89.
- (17) Santana, M. H. P.; De Faria, L. A. Oxygen and chlorine evolution on RuO₂+TiO₂+CeO₂+Nb₂O₅ mixed oxide electrodes. *Electrochimica Acta* **2006**, *51* (17), 3578-3585.
- (18) Kronawitter, C. X.; Vayssieres, L.; Shen, S. H.; Guo, L. J.; Wheeler, D. A.; Zhang, J. Z.; Antoun, B. R.; Mao, S. S. A perspective on solar-driven water splitting with all-oxide hetero-nanostructures. *Energy & Environmental Science* **2011**, *4* (10), 3889-3899.
- (19) Hoffmann, M. R.; Martin, S. T.; Choi, W. Y.; Bahnemann, D. W. Environmental applications of semiconductor photocatalysis. *Chemical Reviews* **1995**, *95* (1), 69-96.
- (20) Kesselman, J. M.; Weres, O.; Lewis, N. S.; Hoffmann, M. R. Electrochemical production of hydroxyl radical at polycrystalline Nb-doped TiO₂ electrodes and

- estimation of the partitioning between hydroxyl radical and direct hole oxidation pathways. *Journal of Physical Chemistry B* **1997**, *101* (14), 2637-2643.
- (21) Gujar, T. P.; Shinde, V. R.; Lokhande, C. D.; Han, S. H. Electrosynthesis of Bi₂O₃ thin films and their use in electrochemical supercapacitors. *Journal of Power Sources* **2006**, *161* (2), 1479-1485.
- (22) Yuan, D.; Zeng, J.; Kristian, N.; Wang, Y.; Wang, X. Bi₂O₃ deposited on highly ordered mesoporous carbon for supercapacitors. *Electrochemistry Communications* **2009**, *11* (2), 313-317.
- (23) Shuk, P.; Wiemhofer, H. D.; Guth, U.; Gopel, W.; Greenblatt, M. Oxide ion conducting solid electrolytes based on Bi₂O₃. *Solid State Ionics* **1996**, *89* (3-4), 179-196.
- (24) Tahar, N. B.; Savall, A. Electrochemical degradation of phenol in aqueous solution on bismuth doped lead dioxide: a comparison of the activities of various electrode formulations. *Journal of Applied Electrochemistry* **1999**, *29* (3), 277-283.
- (25) Tomita, K.; Petrykin, V.; Kobayashi, M.; Shiro, M.; Yoshimura, M.; Kakihana, M. A water-soluble titanium complex for the selective synthesis of nanocrystalline brookite, rutile, and anatase by a hydrothermal method. *Angewandte Chemie-International Edition* **2006**, *45* (15), 2378-2381.
- (26) Gao, Y. F.; Masuda, Y.; Peng, Z. F.; Yonezawa, T.; Koumoto, K. Room temperature deposition of a TiO₂ thin film from aqueous peroxotitanate solution. *Journal of Materials Chemistry* **2003**, *13* (3), 608-613.
- (27) Van de Velde, N.; Arin, M.; Lommens, P.; Poelman, D.; Van Driessche, I. Characterization of the aqueous peroxomethod for the synthesis of transparent TiO₂ thin films. *Thin Solid Films* **2011**, *519* (11), 3475-3479.
- (28) Kraft, A.; Stadelmann, M.; Blaschke, M.; Kreysig, D.; Sandt, B.; Schroder, F.; Rennau, J. Electrochemical water disinfection - Part I: Hypochlorite production from very dilute chloride solutions. *Journal of Applied Electrochemistry* **1999**, *29* (7), 861-868.
- (29) Hanaor, D. A. H.; Sorrell, C. C. Review of the anatase to rutile phase transformation. *Journal of Materials Science* **2011**, *46* (4), 855-874.

- (30) Ardizzone, S.; Bianchi, C. L.; Cappelletti, G.; Ionita, M.; Minguzzi, A.; Rondinini, S.; Vertova, A. Composite ternary SnO₂-IrO₂-Ta₂O₅ oxide electrocatalysts. *Journal of Electroanalytical Chemistry* **2006**, *589* (1), 160-166.
- (31) Connor, P. A.; Dobson, K. D.; McQuillan, A. J. Infrared spectroscopy of the TiO₂/aqueous solution interface. *Langmuir* **1999**, *15* (7), 2402-2408.
- (32) Hu, J. M.; Zhang, J. Q.; Cao, C. N. Oxygen evolution reaction on IrO₂-based DSA^(R) type electrodes: kinetics analysis of Tafel lines and EIS. *International Journal of Hydrogen Energy* **2004**, *29* (8), 791-797.
- (33) Zhang, J. J.; Hu, J. M.; Zhang, J. Q.; Cao, C. N. IrO₂-SiO₂ binary oxide films: Geometric or kinetic interpretation of the improved electrocatalytic activity for the oxygen evolution reaction. *International Journal of Hydrogen Energy* **2011**, *36* (9), 5218-5226.
- (34) Kotz, R.; Stucki, S. Stabilization of RuO₂ by IrO₂ for anodic oxygen evolution in acid-media. *Electrochimica Acta* **1986**, *31* (10), 1311-1316.
- (35) Cooper, K. R.; Smith, M. Electrical test methods for on-line fuel cell ohmic resistance measurement. *Journal of Power Sources* **2006**, *160* (2), 1088-1095.
- (36) Hou, Y. Y.; Hu, J. M.; Liu, L.; Zhang, J. Q.; Cao, C. N. Effect of calcination temperature on electrocatalytic activities of Ti/IrO₂ electrodes in methanol aqueous solutions. *Electrochimica Acta* **2006**, *51* (28), 6258-6267.
- (37) Zhou, X. L.; Ye, Z. G.; Hua, X. Z.; Zou, A. H.; Dong, Y. H. Electrocatalytic activity and stability of Ti/IrO₂ + MnO₂ anode in 0.5 M NaCl solution. *Journal of Solid State Electrochemistry* **2010**, *14* (7), 1213-1219.
- (38) Xu, J. Y.; Liu, G. Y.; Li, J. L.; Wang, X. D. The electrocatalytic properties of an IrO₂/SnO₂ catalyst using SnO₂ as a support and an assisting reagent for the oxygen evolution reaction. *Electrochimica Acta* **2012**, *59*, 105-112.
- (39) Hameed, A.; Montini, T.; Gombac, V.; Fornasiero, P. Surface phases and photocatalytic activity correlation of Bi₂O₃/Bi₂O_{4-x} nanocomposite. *Journal of the American Chemical Society* **2008**, *130* (30), 9658-+.
- (40) Trasatti, S. Progress in the understanding of the mechanism of chlorine evolution at oxide electrodes. *Electrochimica Acta* **1987**, *32* (3), 369-382.

- (41) Park, H.; Vecitis, C. D.; Hoffmann, M. R. Electrochemical water splitting coupled with organic compound oxidation: The role of active chlorine species. *Journal of Physical Chemistry C* **2009**, *113* (18), 7935-7945.
- (42) Muff, J.; Bennedsen, L. R.; Sogaard, E. G. Study of electrochemical bleaching of p-nitrosodimethylaniline and its role as hydroxyl radical probe compound. *Journal of Applied Electrochemistry* **2011**, *41* (5), 599-607.
- (43) Neta, P.; Huie, R. E.; Ross, A. B. Rate constants for reactions of inorganic radicals in aqueous-solution. *Journal of Physical and Chemical Reference Data* **1988**, *17* (3), 1027-1284.
- (44) Pourbaix, M., *Atlas of electrochemical equilibria in aqueous solutions*. 2nd English ed.; National Association of Corrosion Engineers: Houston, Tex., **1974**.
- (45) Sarma, B.; Jurovitzki, A. L.; Smith, Y. R.; Mohanty, S. K.; Misra, M. Redox-induced enhancement in interfacial capacitance of the titania nanotube/bismuth oxide composite electrode. *ACS Applied Materials & Interfaces* **2013**, *5* (5), 1688-1697.
- (46) Kosmulski, M. Compilation of PZC and IEP of sparingly soluble metal oxides and hydroxides from literature. *Advances in Colloid and Interface Science* **2009**, *152* (1-2), 14-25.
- (47) Shamaila, S.; Sajjad, A. K. L.; Chen, F.; Zhang, J. L. Study on highly visible light active Bi₂O₃ loaded ordered mesoporous titania. *Applied Catalysis B-Environmental* **2010**, *94* (3-4), 272-280.
- (48) Bagwasi, S.; Niu, Y. X.; Nasir, M.; Tian, B. Z.; Zhang, J. L. The study of visible light active bismuth modified nitrogen doped titanium dioxide photocatalysts: Role of bismuth. *Applied Surface Science* **2013**, *264*, 139-147.
- (49) Da Silva, L. M.; Boodts, J. F. C.; De Faria, L. A. Oxygen evolution at RuO₂(x) plus Co₃O₄(1-x) electrodes from acid solution. *Electrochimica Acta* **2001**, *46* (9), 1369-1375.